

LA-UR-19-30913

Approved for public release; distribution is unlimited.

Title: Towards an Analysis of the GhostFluid Method

Author(s): Quirk, James J.

Intended for: Report

Issued: 2019-10-25

Disclaimer:

Los Alamos National Laboratory, an affirmative action/equal opportunity employer, is operated by Triad National Security, LLC for the National Nuclear Security Administration of U.S. Department of Energy under contract 89233218CNA000001. By approving this article, the publisher recognizes that the U.S. Government retains nonexclusive, royalty-free license to publish or reproduce the published form of this contribution, or to allow others to do so, for U.S. Government purposes. Los Alamos National Laboratory requests that the publisher identify this article as work performed under the auspices of the U.S. Department of Energy. Los Alamos National Laboratory strongly supports academic freedom and a researcher's right to publish; as an institution, however, the Laboratory does not endorse the viewpoint of a publication or guarantee its technical correctness.

Towards an Analysis of the *GhostFluid* Method

James J. Quirk

June 28, 2006

Abstract

This note presents a Riemann-based analysis of the *GhostFluid* method, applied in one spatial dimension. As it stands, the analysis should be considered a work in progress and open to group discussion.

1 The *GhostFluid* Premise

The *GhostFluid* method is built on the premise that a material interface, such as that shown in Figure 1 (a), can be discretized as two distinct materials that communicate, indirectly, via ghostcells. The situation is shown pictorially in Figure 1 (b). The attraction of the approach is that the two halves of the problem can be integrated using a regular, single material scheme, with none of the complex, book-keeping normally associated with a multi-material solver. On the down side, the reliability of the approach rests with the filling of the ghost states. Specifically, the states must be chosen such that the resultant evolution is consistent with the full problem, and for non-linear systems, there is no guarantee that satisfactory states actually exist.

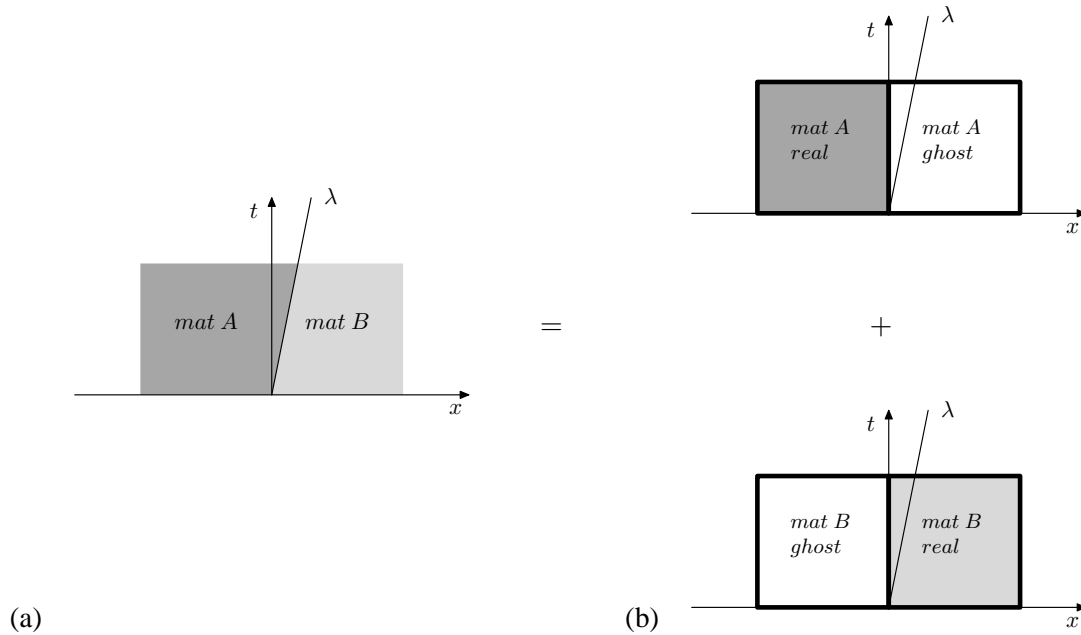


Figure 1: The *GhostFluid* premise: the full problem (a) is broken down to two component problems (b) that are coupled via ghostcells.

1.1 One name, many approaches

It is important to realise that the term “*GhostFluid* method” covers a class of numerical scheme, and it is the details of the ghost-state prescription that defines a particular algorithm. The original *GhostFluid* paper[1], for instance, employed the prescription shown in Figure 2 (a), but some authors prefer the recipe shown in Figure 2 (b), presumably on the grounds that it is easier to implement for non-ideal equations of state. Both prescriptions are justified, by their proponents, on the basis that pressure and velocity are continuous across a contact wave. But this argument is misleading, for in a hydro-simulation acoustic waves can propagate across a material interface and so impose gradients on the local pressure and velocity fields.

The purpose of this note is to examine the *GhostFluid* method from first principles so as to understand how the choice of ghost-states influences the accuracy and robustness of the resultant evolution scheme. Godunov’s Riemann-based approach is adopted, as it provides a clean framework for analysis. Interestingly, the prescription in Figure 2 (a) mimics the Riemann solution in the case of an isolated acoustic wave crossing the material interface, and so while it is usually referred to as an *isobaric* prescription it is better thought of as an *isentropic-coupling*. The prescription in Figure 2 (b) is referred to as *contact-coupling*, for it mimics the Riemann solution only in the case of an isolated contact wave.

For an isolated contact, $P_a = P_b$, and the isobaric-coupling reduces to the contact-coupling. But in general, the performance of the two couplings is different, and so their usual justification, which does not distinguish between the couplings, is clearly incomplete. Indeed, later on, we will show that the contact-coupling is actually inconsistent with the underlying PDE’s and as a consequence should be avoided.

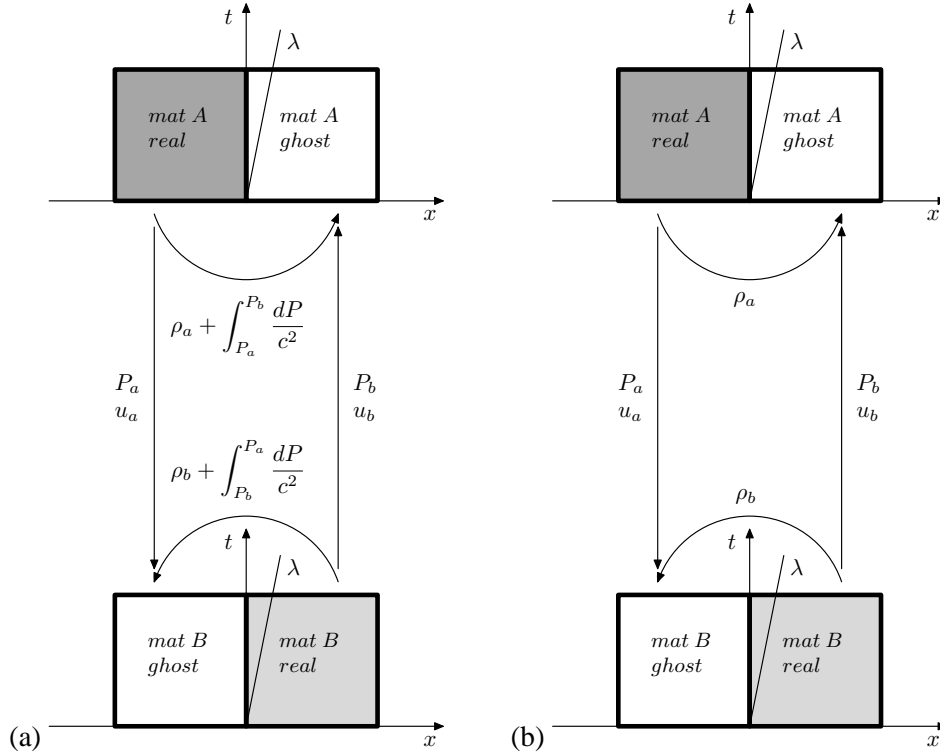


Figure 2: Two *GhostFluid* prescriptions in common use. (a) is the *isobaric* approach used in[1] where the pressure, P , and velocity, u , in a ghost-cell are copied from the co-located real material. And the density, ρ , is found by connecting the nearest real-cell, of the same material, by the isentrope $c^2 = \frac{\partial P}{\partial \rho}$. (b) is a variation on a theme, where P and u are the same as the isobaric case, and density is found by simple extrapolation.

2 Sources of Error

The aim of this note is to develop an understanding of the error associated with the *GhostFluid* coupling. Godunov's Riemann-based approach is adopted, as it provides a clean framework for analysis.

2.1 Choice of control volumes

Consider Figure 3, it shows the Riemann solution that arises when a diaphragm, separating two semi-infinite states, \mathbf{W}_L^n and \mathbf{W}_R^n , bursts. In the general case, three waves separate four states. The idea behind Godunov's method is to average the Riemann solution to find the numerical solution at time t^{n+1} , and although originally developed for a single material, the method extends trivially to two materials. Specifically,

$$\begin{aligned} C'b\mathbf{W}_L^{n+1} &= C'a\mathbf{W}_L^n + ab\mathbf{W}_{*L}^n \\ bC\mathbf{W}_R^{n+1} &= bc\mathbf{W}_{*R}^n + cC\mathbf{W}_R^n \end{aligned} \quad (1)$$

which can be re-written in term of Courant numbers, $\nu = \frac{\lambda \Delta t}{\Delta x}$, to get:

$$\begin{aligned} (1 + \nu_2)\mathbf{W}_L^{n+1} &= (1 + \nu_1)\mathbf{W}_L^n + (\nu_2 - \nu_1)\mathbf{W}_{*L}^n \\ (1 - \nu_2)\mathbf{W}_R^{n+1} &= (\nu_3 - \nu_2)\mathbf{W}_{*R}^n + (1 - \nu_3)\mathbf{W}_R^n \end{aligned} \quad (2)$$

Equation 2 can also be derived using a finite-volume formulation. In conservation form, the governing equations can be written:

$$\begin{aligned} \frac{\partial \mathbf{W}}{\partial t} + \frac{\partial \mathbf{F}}{\partial x} &= 0 \\ \mathbf{F} &= \mathbf{F}(\mathbf{W}(x, t)) \end{aligned} \quad (3)$$

which can be integrated for the volumes $AbC'B'$ and $ABCb$. Consider the right-hand volume:

$$\begin{aligned} (1 - \nu_2)\mathbf{W}_R^{n+1} &= \mathbf{W}_R^n - \frac{\Delta t}{\Delta x}(\bar{\mathbf{F}}_{BC} - \bar{\mathbf{F}}_{Ab}) \\ \bar{\mathbf{F}}_{BC} &= \mathbf{F}(\mathbf{W}_R^n) \\ \bar{\mathbf{F}}_{Ab} &= \mathbf{F}(\mathbf{W}_{*R}^n) - \lambda_2 \mathbf{W}_{*R}^n \end{aligned} \quad (4)$$

which since,

$$\mathbf{F}(\mathbf{W}_R^n) - \mathbf{F}(\mathbf{W}_{*R}^n) = \lambda_3(\mathbf{W}_R^n - \mathbf{W}_{*R}^n) \quad (5)$$

can be rearranged to match Equation 2. The left-hand volume can be handled in the same way.

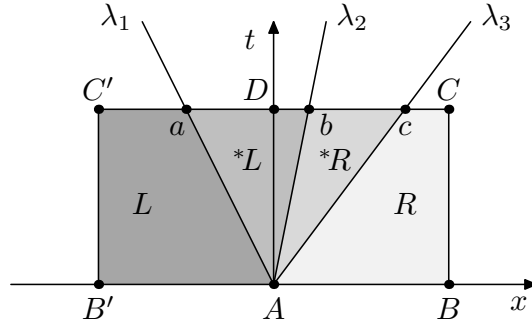


Figure 3: A diaphragm separating two semi-infinite states bursts. The Riemann solution, in the general case, consists of three waves, with speeds $\{\lambda_1, \lambda_2, \lambda_3\}$, that separate four states $\{\mathbf{W}_L, \mathbf{W}_{*L}, \mathbf{W}_{*R}, \mathbf{W}_R\}$.

The Riemann solution provides motivation for the *GhostFluid* coupling shown in Figure 4. However, a key element of the *GhostFluid* method is that the single-material solvers operate on the fixed control-volumes, $ABCD$ and $ADC'B'$, instead of the time-varying volumes bounded by the contact wave. Thus,

$$\begin{aligned}
\mathbf{W}_L^{n+1} &= \mathbf{W}_L^n - \frac{\Delta t}{\Delta x} (\bar{\mathbf{F}}_{AD} - \bar{\mathbf{F}}_{B'C'}) \\
\bar{\mathbf{F}}_{AD} &= \mathbf{F}(\mathbf{W}_{*L}^n) \quad \text{for } \lambda_1 < 0 \\
\bar{\mathbf{F}}_{AD} &= \mathbf{F}(\mathbf{W}_L^n) \quad \text{for } \lambda_1 > 0 \\
\bar{\mathbf{F}}_{B'C'} &= \mathbf{F}(\mathbf{W}_L^n) \\
\mathbf{W}_R^{n+1} &= \mathbf{W}_R^n - \frac{\Delta t}{\Delta x} (\bar{\mathbf{F}}_{BC} - \bar{\mathbf{F}}_{AD}) \\
\bar{\mathbf{F}}_{BC} &= \mathbf{F}(\mathbf{W}_R^n) \\
\bar{\mathbf{F}}_{AD} &= \mathbf{F}(\mathbf{W}_{*R}^n) \quad \text{for } \lambda_3 > 0 \\
\bar{\mathbf{F}}_{AD} &= \mathbf{F}(\mathbf{W}_R^n) \quad \text{for } \lambda_3 < 0
\end{aligned} \tag{6}$$

which can be rearranged to give:

$$\begin{aligned}
\mathbf{W}_L^{n+1} &= \mathbf{W}_L^n - \nu'_1 (\mathbf{W}_{*L}^n - \mathbf{W}_L^n) \\
\mathbf{W}_R^{n+1} &= \mathbf{W}_R^n - \nu'_3 (\mathbf{W}_R^n - \mathbf{W}_{*R}^n)
\end{aligned} \tag{7}$$

where:

$$\begin{aligned}
\nu'_1 &= \min(0, \nu_1) \\
\nu'_3 &= \max(0, \nu_3)
\end{aligned}$$

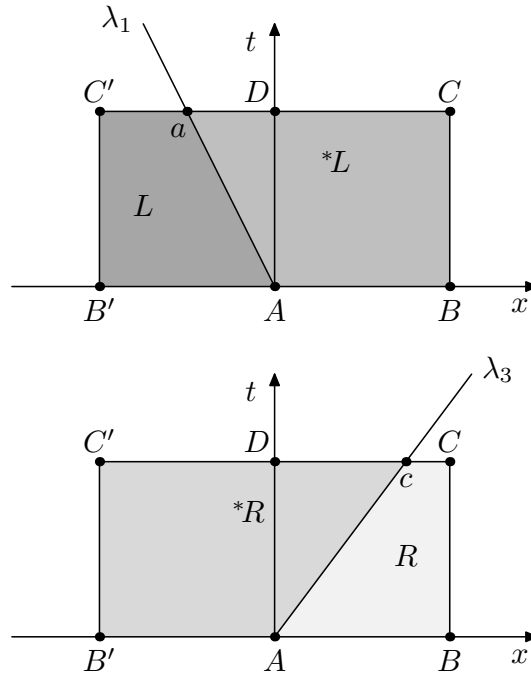


Figure 4: *GhostFluid* coupling motivated by the Riemann solution.

Now the departure of Equation 7 from Equation 2 can be used to gauge the *GhostFluid* error that arises from using fixed control-volumes. For ignoring the complication of integrating through an expansion fan, Equation 2 provides the exact evolution for the states that abutt the interface. To make the comparison easier, Equation 2 can be rearranged to give:

$$\begin{aligned}\mathbf{W}_L^{n+1} &= \mathbf{W}_L^n - \left(\nu'_1 - \frac{\nu'_2(1 + \nu'_1)}{(1 + \nu'_2)} \right) (\mathbf{W}_{*L}^n - \mathbf{W}_L^n) \\ \mathbf{W}_R^{n+1} &= \mathbf{W}_R^n - \left(\nu'_3 - \frac{\nu''_2(1 - \nu'_3)}{(1 - \nu''_2)} \right) (\mathbf{W}_R^n - \mathbf{W}_{*R}^n)\end{aligned}\quad (8)$$

where the left and right states at t^{n+1} are now for the Eulerian cells $ABCD$ and $AB'C'D$, and:

$$\begin{aligned}\nu'_2 &= \min(0, \nu_2) \\ \nu''_2 &= \max(0, \nu_2)\end{aligned}$$

Thus the errors can be written:

$$\begin{aligned}\epsilon_L^{n+1} &= \frac{\nu'_2(1 + \nu'_1)}{(1 + \nu'_2)} (\mathbf{W}_{*L}^n - \mathbf{W}_L^n) \\ \epsilon_R^{n+1} &= -\frac{\nu''_2(1 - \nu'_3)}{(1 - \nu''_2)} (\mathbf{W}_R^n - \mathbf{W}_{*R}^n)\end{aligned}\quad (9)$$

Equation 9 suggests that the error which arises from using a fixed-control volume will be small:

- For an isolated contact, $\mathbf{W}_{*L}^n = \mathbf{W}_L^n$ and $\mathbf{W}_R^n = \mathbf{W}_{*R}^n$, so $\epsilon_L^{n+1} = \epsilon_R^{n+1} = 0$.
- For flow to the right $\nu'_2 = 0$, so $\epsilon_L^{n+1} = 0$.
- For flow to the left $\nu''_2 = 0$, so $\epsilon_R^{n+1} = 0$.
- For a strong shock moving to the left, $\nu'_1 \rightarrow -1$, so $\epsilon_L^{n+1} \rightarrow 0$.
- For a strong shock moving to the right, $\nu'_3 \rightarrow 1$, so $\epsilon_R^{n+1} \rightarrow 0$.
- For subsonic flow, both ν'_2 and ν''_2 are small, so $\epsilon_L^{n+1} \rightarrow 0$ and $\epsilon_R^{n+1} \rightarrow 0$.

Heuristic arguments such as the above can prove to be misleading, or even downright dangerous. But in Section 3, computational results will be presented to support the basic assertions.

It is pertinent to ask where the errors will be largest, but given the non-linearities involved the answer is not straightforward. For example, the larger jump, $(\mathbf{W}_R^n - \mathbf{W}_{*R}^n)$, the smaller the quantity $1 - \nu_3$ (assuming a fixed Δt); and vice versa. Therefore the error is to some degree self-adjusting. Similarly, reducing the time step: increases $1 - \nu_3$, but decreases ν'_2 . If ν'_2 is assumed to be small, which implies ν'_2 is small, then the errors can be expanded to:

$$\begin{aligned}\epsilon_L^{n+1} &= \nu'_2(1 + \nu'_1)(\mathbf{W}_{*L}^n - \mathbf{W}_L^n) \\ \epsilon_R^{n+1} &= \nu''_2(1 - \nu'_3)(\mathbf{W}_R^n - \mathbf{W}_{*R}^n)\end{aligned}$$

from which it can be seen that the maximum errors are:

$$\begin{aligned}\epsilon_L^{max} &= \nu'_2(\mathbf{W}_{*L}^n - \mathbf{W}_L^n) \\ \epsilon_R^{max} &= \nu''_2(\mathbf{W}_R^n - \mathbf{W}_{*R}^n)\end{aligned}$$

which, given the starting assumption, are small.

It is also pertinent to ask how do the errors accumulate over multiple time steps. But, again, this is not an easy question to answer. The worst case situation is that repeated small errors accumulate to become large errors. In this regard, an expansion crossing a material interface is likely to result in a larger error accumulation than a shock crossing the interface. But the computational evidence is that the errors do not accumulate when using the Riemann-based, *GhostFluid* coupling.

2.2 Lack of sub-cell resolution

The *GhostFluid* method does not employ sub-cell resolution. Consequently it is possible for a cell to flip materials for small changes in the level-set used to track the material interface. Consider, for example, Figure 5.

The top-half of the plot shows the set-up when the material interface is positioned just to the left of the midpoint of the cell $ABCD$. The Riemann solver coupling, discussed in the previous section, would require that \mathbf{W}_{*L}^n be painted into the cell $ABCD$. Now at the end of the time step, the interface will have moved past the midpoint. Consequently, for the next time step, cell $ABCD$ will be considered to be a real material and it is the cell $BEFC$ that will receive a ghost-state. This introduces an error, as the cell $ABCD$ has not been updated for the left-hand material. From the Riemann analysis the cell should have the state \mathbf{W}_L^{n+1} , but it is left with the ghost state, \mathbf{W}_{*L}^n . Depending on the gradients in the problem, this error can be large, but it is a sporadic error and so is likely to be less important than a persistent error. It should also be noted that the error can be removed with the addition of a fix-up pass. One that explicitly populates a cell, containing a newly emerged material, with the appropriate neighbouring state.

The lack of sub-cell resolution also means that as a material interface propagates through the mesh, it is artificially kept behind the true position for the first-half of its transit across a cell, only to jump ahead of the true position for the second-half of the transit. Now for linear problems one can imagine how the resultant errors would be self-cancelling, thus resulting in a simulation which is correct, in some average sense. But for a non-linear problem, it is likely that the errors would not cancel and so leave some imprint on the numerical solution. While this situation has not yet been analysed, one can ask what happens to the Riemann solution as λ_2 is perturbed.

For instance, if λ_2 is artificially slowed, \mathbf{W}_R^{n+1} is weighted towards \mathbf{W}_{*R}^n , and when λ_2 is artificially accelerated, \mathbf{W}_R^{n+1} is weighted towards \mathbf{W}_R^n . Thus for an expansion wave crossing the material interface, the density for the first-half of the transit would be expected to be on the low side, and for the second-half of the transit it would be expected to be on the high side. For a shock wave crossing the material interface, the situation is reversed. It is too early to tell whether or not such reasoning has any merit. But the possibility that the *GhostFluid* method can introduce artificial expansions and compressions, by its lack of sub-cell resolution, should not be dismissed out of hand.

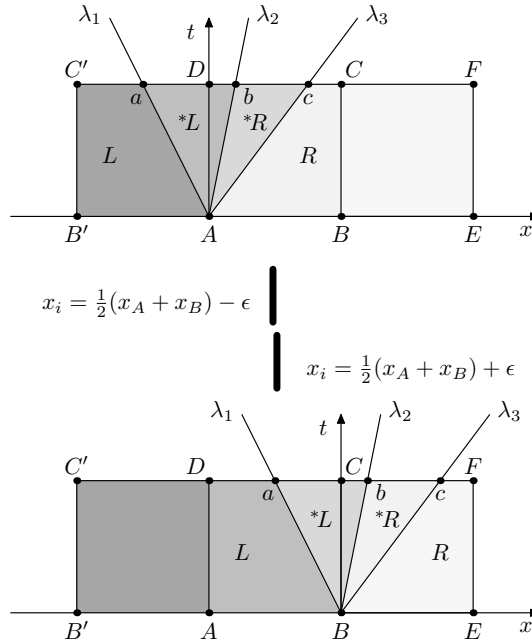


Figure 5: A small change in the material interface position can flip the material in a cell. Here, cell $ABCD$ changes material as the interface crosses the cell's mid-point.

2.3 Choice of *GhostFluid* states

In the context of the present analysis the ghost states are not open to choice as the Riemann solution is the exact solution to the governing PDE's, and the “star states” are what couple the two materials. But since other *GhostFluid* prescriptions are in use, one can analyze the error associated with a particular recipe by examining the departure of the states it uses from those used in the Riemann-based coupling.

Consider, for example, Figure 6. It shows one *GhostFluid* prescription in common usage. This prescription mimics the Riemann solution only in the case of an isolated contact wave, and so when gradients are introduced at the material interface, owing to either the passage of a shock wave or an expansion fan, the ghost states will be in error.

Although the Riemann solution cannot be written in closed form, at least not in the general case, a linearized solution can be formulated:

$$\begin{aligned}
U_* &= \frac{P_L - P_R + Z_L U_L + Z_R U_R}{Z_L + Z_R} \\
P_* &= \frac{(U_L - U_R) Z_L Z_R + Z_L P_R + Z_R P_L}{Z_L + Z_R} \\
\rho_{*L} &= \rho_L + \frac{\bar{\rho}_L (U_L - U_*)}{\bar{c}_L} \\
\rho_{*R} &= \rho_R + \frac{\bar{\rho}_R (U_* - U_R)}{\bar{c}_R}
\end{aligned} \tag{10}$$

where,

$$\begin{aligned} Z_L &= \bar{\rho}_L \bar{c}_L \\ Z_R &= \bar{\rho}_R \bar{c}_R \end{aligned}$$

The average quantities $\bar{\rho}_L$, $\bar{\rho}_R$, \bar{c}_L , and \bar{c}_R need to be chosen so as to endow certain properties on the linearized solution. For instance, in the single-material case, where $\bar{\rho}_L = \bar{\rho}_R = \bar{\rho}$ and $\bar{c}_L = \bar{c}_R = \bar{c}$, so-called ‘‘Roe averages’’ ensure that the linearized solution mimics the exact Riemann solution for an isolated shock[3, 4, 5]. In the two-material case, the common choice is to use:

$$\begin{aligned}\bar{\rho}_L &= \rho_L \\ \bar{\rho}_R &= \rho_R \\ \bar{c}_L &= c_L \\ \bar{c}_R &= c_R\end{aligned}\tag{11}$$

which has no special merit, except that it is straightforward to implement.

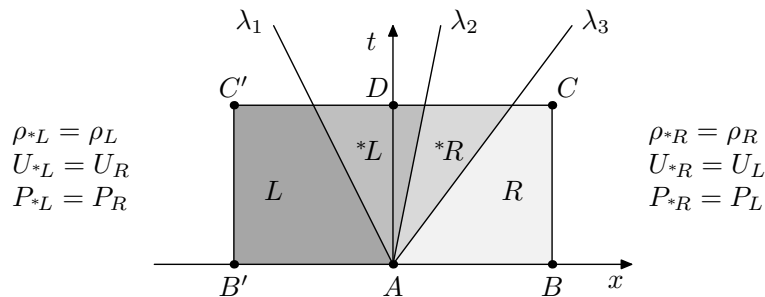
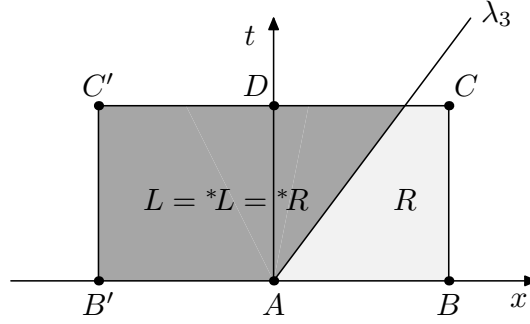


Figure 6: One *GhostFluid* prescription in common usage. This prescription can be termed *contact-coupling* as it mimics the Riemann solution in the case of an isolated contact surface.

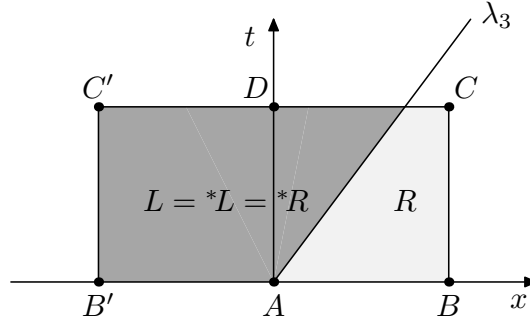
Equation 10 can be used to gauge the accuracy of the contact-coupling prescription shown in Figure 6. For instance, the contact-coupling clearly under-estimates P_* when $(P_L = P_R, U_R = -U_L)$. However, the likelihood of flow colliding at a material interface is small. A much more common occurrence would be either a shock wave or an expansion fan moving through the interface. In the case of a shock moving to the right:

$$\begin{aligned}\rho_L &= \rho^*_L = \rho^*_R > \rho_R \\ P_L &= P_* > P_R \\ U_L &= U_* > U_R\end{aligned}$$



while for an expansion:

$$\begin{aligned}P_L &= P_* < P_R \\ \rho_L &= \rho^*_L = \rho^*_R < \rho_R \\ U_L &= U_* < U_R\end{aligned}$$



In both these cases the contact-coupling prescribes:

$$\begin{aligned}\rho^*_L &= \rho_L \\ U^*_L &= U_R \\ P^*_L &= P_R \\ \rho^*_R &= \rho_R \\ U^*_R &= U_L \\ P^*_R &= P_L\end{aligned}$$

and so it fails to mimic the essential flow attributes. Note that there is also a lack of consistency, for:

$$\begin{aligned}P^*_L &\neq P^*_R \\ U^*_L &\neq U^*_R\end{aligned}$$

In the next section we present numerical results to demonstrate that the contact-coupling approach is indeed found wanting in these circumstances.

3 Consistency Check

A consistency check of the *GhostFluid* method can be performed by comparing a single-material simulation against a two-material simulation where the two materials are the same. This is not how the *GhostFluid* method would be used in practice, but in the limit of the left- and right- materials being the same, the *GhostFluid* method should not undermine the base flow-solver used for the simulation.

Two cases are presented below. The first case examines what affect the *GhostFluid* coupling has when an expansion fan crosses a material interface. The second looks at a shock wave crossing the interface. Results are presented for both types of *GhostFluid* coupling discussed here: the Riemann-coupling from Section 2.1 and the contact-coupling from Figure 6.

3.1 Smooth flows

First we consider an isolated interface in a smooth flow, with states $()_L$ and $()_R$ across the interface. As the flow is smooth, we can use the single-material, Euler equations cast in terms of the primitive variables: density, ρ , velocity, u , pressure, P , and the ratio of specific heats, γ . Thus the governing equations are:

$$\frac{\partial \mathbf{U}}{\partial t} + \mathbf{A} \frac{\partial \mathbf{U}}{\partial x} = 0 \quad (12)$$

where:

$$\mathbf{U} = \begin{pmatrix} \rho \\ u \\ P \end{pmatrix}; \quad \mathbf{A} = \begin{pmatrix} u & \rho & 0 \\ 0 & u & 1/\rho \\ 0 & \gamma P & u \end{pmatrix} \quad (13)$$

Applying a Roe-type[3, 4, 5] linearization to Equation 12, we get wave-speeds $\{\tilde{\lambda}_1, \tilde{\lambda}_2, \tilde{\lambda}_3\}$:

$$\tilde{\lambda}_1 = \tilde{u} - \tilde{a}; \quad \tilde{\lambda}_2 = \tilde{u}; \quad \tilde{\lambda}_3 = \tilde{u} + \tilde{a} \quad (14)$$

wave-strengths $\{\tilde{\alpha}_1, \tilde{\alpha}_2, \tilde{\alpha}_3\}$:

$$\tilde{\alpha}_1 = \frac{\Delta P - \tilde{\rho} \tilde{a} \Delta u}{2 \tilde{\rho} \tilde{a}^2}; \quad \tilde{\alpha}_2 = \frac{\tilde{a}^2 \Delta \rho - \Delta P}{\tilde{\rho} \tilde{a}^2}; \quad \tilde{\alpha}_3 = \frac{\Delta P + \tilde{\rho} \tilde{a} \Delta u}{2 \tilde{\rho} \tilde{a}^2}; \quad (15)$$

and right eigenvectors $\{\tilde{\mathbf{e}}_1, \tilde{\mathbf{e}}_2, \tilde{\mathbf{e}}_3\}$:

$$\tilde{\mathbf{e}}_1 = \begin{pmatrix} \tilde{\rho} \\ -\tilde{a} \\ \tilde{\rho} \tilde{a}^2 \end{pmatrix}; \quad \tilde{\mathbf{e}}_2 = \begin{pmatrix} \tilde{\rho} \\ 0 \\ 0 \end{pmatrix}; \quad \tilde{\mathbf{e}}_3 = \begin{pmatrix} \tilde{\rho} \\ \tilde{a} \\ \tilde{\rho} \tilde{a}^2 \end{pmatrix}; \quad (16)$$

Here a is the sound speed, $\frac{\gamma P}{\rho}$, $\Delta()$ denotes the jump $()_R - ()_L$ across the interface, and $\tilde{()}$ denotes some average of the $()_L$ and $()_R$ states. Note, by construction:

$$\Delta \mathbf{U} = \sum_{k=1}^{k=3} \tilde{\alpha}_k \tilde{\mathbf{e}}_k \quad (17)$$

We can interpret Equations 14 through 16 in terms of the Riemann solution shown in Figure 7. The eigenvectors give the proportional jumps in the primitive variables, $\{\rho, u, P\}$, across each wave. The wave strengths then give the scaling in the jumps. Note that the linearization collapses each wave down to a single characteristic which is not a good approximation for a strong expansion fan, where it is possible for the lead and trailing characteristics to be moving in opposite directions i.e. the fan contains a sonic point. However, for the purposes of the present analysis, we can ignore this particular complication. Here, we are also assuming that the flow is smooth and so $\tilde{\lambda}_1$ and $\tilde{\lambda}_3$ are not shock waves.

The idea is that we can now use the linearized evolution to evaluate the three *GhostFluid* prescriptions shown in Figure 8. Specifically, we can ask whether or not the coupling introduced by a particular choice of ghost-states results in an evolution that mimics the single-material evolution. If it does not then it can be argued that the coupling is inconsistent with the governing PDE's. In the first instance, we need only consider the case of single right-going acoustic wave, and the data across the interface is chosen such that $\tilde{\alpha}_1 = \tilde{\alpha}_2 = 0$. This case is shown in Figure 9.

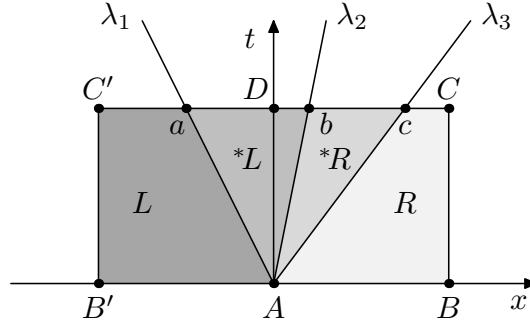
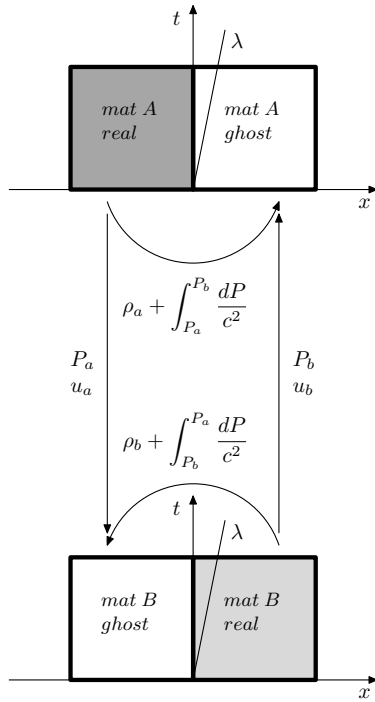
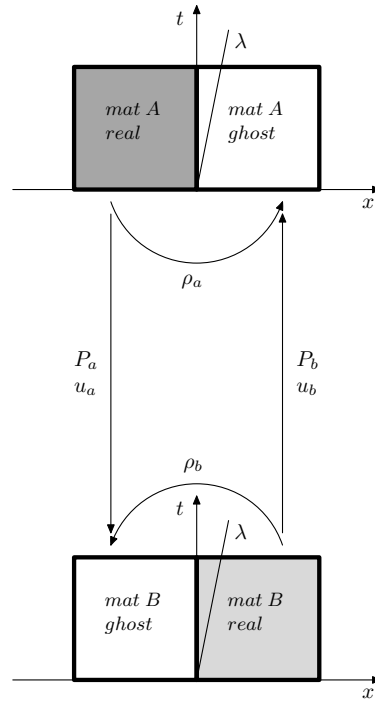


Figure 7: A diaphragm separating two semi-infinite states bursts. The Riemann solution, in the general case, consists of three waves, with speeds $\{\lambda_1, \lambda_2, \lambda_3\}$, that separate four states $\{\mathbf{U}_L, \mathbf{U}_{*L}, \mathbf{U}_{*R}, \mathbf{U}_R\}$.

Isobaric-coupling



Contact-coupling



Riemann-coupling

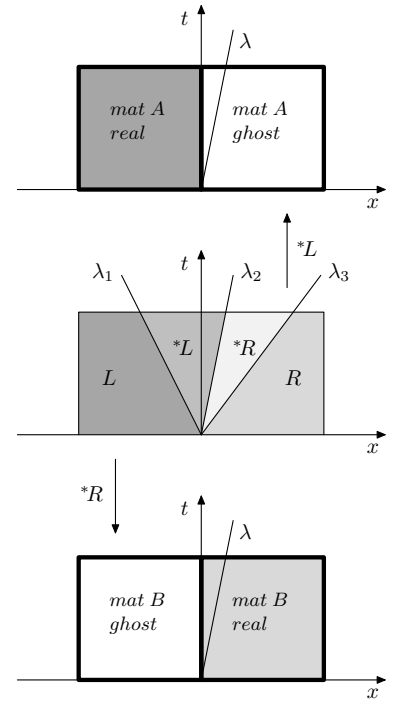


Figure 8: Three prescriptions used by the *GhostFluid* method.

3.1.1 A right-going acoustic wave

If the states either side of the interface are consistent with a single right-going acoustic wave, as shown in Figure 9, then from Equation 15:

$$\Delta P = \tilde{\rho} \tilde{a} \Delta u; \quad \Delta P = \tilde{a}^2 \Delta \rho; \quad (18)$$

and the evolution in the cell $i + 1$ is:

$$\mathbf{U}_{i+1}^{n+1} = \mathbf{U}_{i+1}^n - \tilde{\nu}_3 \tilde{\alpha}_3 \tilde{\mathbf{e}}_3 \quad (19)$$

where $\tilde{\nu}_3$ is the Courant number:

$$\tilde{\nu}_3 = \frac{\tilde{\lambda}_3 \Delta t}{\Delta x} \quad (20)$$

This evolution can be rewritten as:

$$\mathbf{U}_{i+1}^{n+1} = \mathbf{U}_{i+1}^n - \tilde{\nu}_3 \begin{pmatrix} \Delta \rho \\ \Delta u \\ \Delta P \end{pmatrix} \quad (21)$$

to indicate that the primitive variables are simply advected with the appropriate wave speed.

The evolution of the i^{th} cell is similar, but need not be considered further, as it is not affected by the choice of ghost-states. For using a signal-framework[5], only waves that enter a cell affect the cell's evolution, and since here we are assuming a single right-going acoustic wave, the coupling cannot affect the left-hand cell¹.

By inspection, the riemann-coupling is consistent with the single material evolution. For the right-hand material receives the ghost-state, \mathbf{U}_{*R} , which is identical to the left-hand material, \mathbf{U}_L , and so the pseudo-material interface is effectively seamless. This is also the case with the isobaric-coupling. By construction, P and u are simply lifted from the left-hand material, and because here the wave is assumed to be isentropic, the isentropic extrapolation recovers the left-hand density. For this reason, the isobaric-coupling introduced in [1] would be better termed isentropic-coupling. Indeed, by the argument given in[1], the contact-coupling in Figure 8 could also be termed isobaric. But as we show below, it does not result in a seamless interface treatment, and so it is not the constant-pressure element that leads to a well founded coupling.

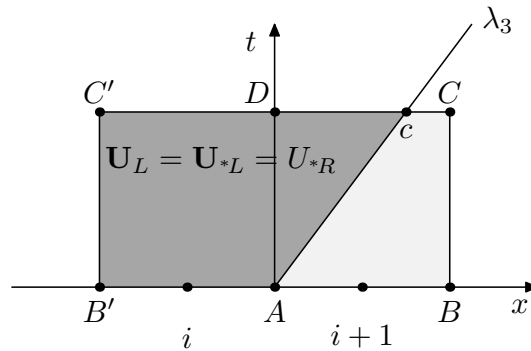


Figure 9: The Riemann solution in the case of a single, right-moving acoustic wave.

¹This statement is only true for a frozen interface. When the interface is allowed to move the solution in the left-hand cell can be contaminated.

The contact-coupling artificially imposes the condition $\Delta\rho = 0$. Thus the wave strength $\tilde{\alpha}_2$ is activated:

$$\tilde{\alpha}_2 = \frac{-\Delta P}{\tilde{\rho}\tilde{a}^2}; \quad (22)$$

and the average quantities $\tilde{\rho}$, \tilde{a} are altered. To leading order, however, the terms $\tilde{\rho}\tilde{a}\Delta u$ and $\tilde{\rho}\tilde{a}^2$ remain the same and so the dominant affect is the spurious activation of the contact wave, as shown in Figure 10.

The evolution in the cell $i + 1$ is now:

$$\mathbf{U}_{i+1}^{n+1} = \mathbf{U}_{i+1}^n - \tilde{\nu}_3 \tilde{\alpha}_3 \tilde{\mathbf{e}}_3 - \tilde{\nu}_2 \tilde{\alpha}_2 \tilde{\mathbf{e}}_2 \quad (23)$$

where $\tilde{\nu}_2$ is the Courant number:

$$\tilde{\nu}_2 = \frac{\tilde{\lambda}_2 \Delta t}{\Delta x} \quad (24)$$

This new evolution can be rewritten as:

$$\mathbf{U}_{i+1}^{n+1} = \mathbf{U}_{i+1}^n - \tilde{\nu}_3 \begin{pmatrix} \Delta\rho \\ \Delta u \\ \Delta P \end{pmatrix} + \tilde{\nu}_2 \begin{pmatrix} \Delta\rho \\ 0 \\ 0 \end{pmatrix} \quad (25)$$

It is tempting to argue that Equation 25 is but a small departure from Equation 21, for $\tilde{\lambda}_3$ is usually much larger than $\tilde{\lambda}_2$. But the numerical evidence is that with repeated applications of the evolution, say as an expansion fan moves through the interface, the error in density accumulates. To understand why this is the case, consider the functional form of Equation 25. There is no error in u or P , only in ρ . Thus after one iteration the velocity and pressure jump across the interface will still be consistent with the acoustic wave fed into the problem. Therefore a second iteration will compound the situation, as will a third, and a fourth, and so on. Now since the error in density affects the quantities $\tilde{\rho}\tilde{a}$ and $\tilde{\rho}\tilde{a}^2$ there will come a point where errors creep into the velocity and pressure fields, but to leading order, $\tilde{\alpha}_3$ remains the same as in the single-material case, thereby allowing the density error to grow in an unbounded fashion.

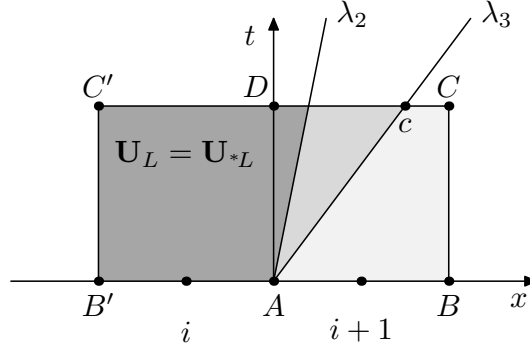


Figure 10: For a right-moving acoustic wave, the contact-coupling artificially activates the contact wave.

3.1.2 Numerical results for a perfect gas

We now present numerical results, for a perfect gas, to demonstrate that the above analysis is essentially correct. Consider the computational setup shown in Figure 11. The idea of this test is to introduce a material interface at point x_i , somewhere in the right-side of the domain, and then use the solution from the left-side as a control to observe the affect of the *GhostFluid* coupling. The initial velocity can also be tuned to alter the strength of the resultant expansion fans. As can be seen from Figures 12-16, the contact-coupling gives markedly poorer results for the density field than either the isobaric- or riemann- couplings. The velocity and pressure profiles, on the other hand, are comparable in the all three cases. Figures 18 and 19 show the evolution of the density step as the expansion-fan crosses the material interface.

The plots of the wave strengths, see Figures 13, 15, and 17, are especially illuminating. Specifically, as is seen with the isobaric- and riemann- couplings, $\tilde{\alpha}_2$ should nominally be zero. But with the contact-coupling, $\tilde{\alpha}_2$ is comparable in strength to $\tilde{\alpha}_3$, thus bearing out the error analysis. In short, the contact-coupling is inconsistent with the underlying PDE's and should not be used. A careful examination of the wave strengths suggests that the isobaric-coupling performs marginally better than the riemann-coupling. While this was unexpected, it should be appreciated that the accuracy of the linearized riemann-solver is ultimately set by its choice of wave speeds, and as noted earlier the present solver is actually quite poor on that score. The important point, however, is that the riemann-coupling preserves the characteristic jumps across waves, and so is automatically consistent with the governing PDE's.

The present test can be rerun using a frozen interface, see Figure 20, and this bears out the observation, given earlier, that the left-hand cell is not affected by the contact-coupling i.e. the error is introduced in the right-hand cell for a right-moving characteristic². With a moving interface, as discussed in §2.2, there is an additional error introduced when a cell flips material. From the numerical evidence, this secondary error seems sufficient to centre the density error about the interface, c.f. Figures 12 and Figures 20.

The computational results shown here are generated by scripts bundled with *amr_sol::multimat*, see:

examples/tests/pg/expansion.1
examples/tests/pg/expansion.2

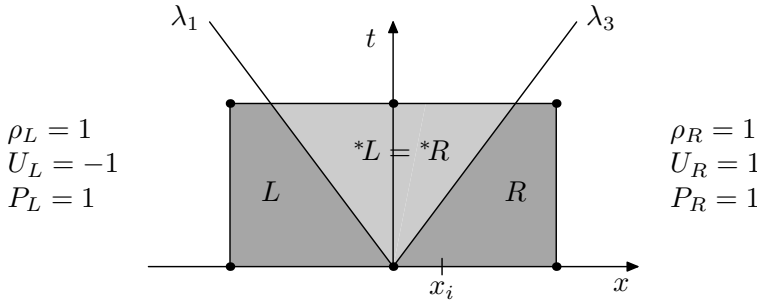


Figure 11: Schematic showing the wave pattern for the expansion test. Note that the expansion fans are collapsed down to a single characteristic, as would be the case with a linearized analysis. The material interface is positioned at $x_i = 0.15$.

isobaric-coupling

contact-coupling

riemann-coupling

Figure 12: Computational results for an expansion-fan crossing a material interface; click to zoom in on the individual graphs. The solid lines are the control solution from the left-hand side of the computational domain. Observe how the *contact-coupling* introduces an unphysical step in the density profile, but the velocity and pressure profiles are unaffected. The *isobaric* and *riemann* couplings give comparable results.

isobaric-coupling

contact-coupling

riemann-coupling

Figure 13: Plots of $\tilde{\alpha}_1$, $\tilde{\alpha}_2$, and $\tilde{\alpha}_3$, for the expansion test. In practice all the couplings activate $\tilde{\alpha}_2$, whereas for a pure expansion it would be expected to be of zero strength. However, in accordance with the analysis, $\tilde{\alpha}_2$ for the contact-coupling is much larger than with the other two couplings. The difference between the isobaric-coupling and riemann-coupling is small.

isobaric-coupling

contact-coupling

riemann-coupling

Figure 14: The same computation as shown in Figure 12, but twice the mesh resolution. The unphysical step in density is reduced in size, however, it is still pronounced. Note that the nature of the error is such that it does not have a simple order of convergence. The error introduced per iteration certainly decreases as the mesh size decreases. But to counteract the reduction, more iterations are needed to reach a given time. Thus it is the accumulation of the error that matters, and inevitably the accumulation is controlled by non-linear effects that are beyond the scope of the present analysis.

isobaric-coupling

contact-coupling

riemann-coupling

Figure 15: Plots of $\tilde{\alpha}_1$, $\tilde{\alpha}_2$, and $\tilde{\alpha}_3$, corresponding to Figure 14. The spurious $\tilde{\alpha}_2$ is two orders of magnitude larger with the contact-coupling than it is with either the isobaric- or riemann- couplings.

isobaric-coupling

contact-coupling

riemann-coupling

Figure 16: The same computation as shown in Figure 12, but four times the mesh resolution. The unphysical density-step is still prominent, suggesting that the *contact-coupling* is deficient.

isobaric-coupling

contact-coupling

riemann-coupling

Figure 17: Plots of $\tilde{\alpha}_1$, $\tilde{\alpha}_2$, and $\tilde{\alpha}_3$, corresponding to Figure 16. The spurious $\tilde{\alpha}_2$ is again two orders of magnitude larger with the contact-coupling than it is with either the isobaric- or riemann- couplings.

Figure 18: The unphysical density-step, introduced by the *contact-coupling*, grows as the expansion-fan crosses the material interface. This time sequence is taken from the simulation shown in Figure 12.

Figure 19: The evolution of the error in density remains the same as the grid is refined. This time sequence is taken from the simulation shown in Figure 16.

isobaric-coupling

contact-coupling

riemann-coupling

Figure 20: Computational results for an expansion-fan crossing a frozen material interface; click to zoom in on the individual graphs. The solid lines are the control solution from the left-hand side of the computational domain. Observe how the *contact-coupling* introduces an unphysical step in the density profile, but the velocity and pressure profiles are unaffected. The *isobaric* and *riemann* couplings give comparable results.

3.1.3 Numerical results PBX-9502

The unphysical density-step introduced by the *contact-coupling* would be expected to be benign for a perfect-gas simulation; an unwanted glitch, but not a show-stopper. On the other hand, for the sorts of equations of state (EOS) used in high-explosive simulations, a perturbation to the density field could conceivably take the numerical simulation outside the EOS’s thermodynamic bounds. Therefore we rerun the test given above, replacing the perfect gas with *PBX-9502*.

The results are shown in Figures 21 through 28. Note that these simulations were run with the reaction turned *off*. The basic behaviour is the same as for the perfect gas case, except now the perturbation introduced by the *contact-coupling* is sufficient to trip the EOS, at least on the coarsest grid run. Thus the simulation cannot run to completion and it fails at the time step immediately following the last frame shown in Figure 21. The failure occurs at the density minimum, with $c^2 < 0$. For the higher resolution grids, see Figures 23 and 25, the *contact coupling* artifact is sufficiently reduced that the simulation can run to completion, but it is clear that the contact-coupling is much inferior to both the isobaric- and riemann- couplings.

Before moving on, it should be noted that the initial conditions chosen here also cause trouble for the base flow-solver with a single material. Specifically, if the velocity is increased slightly beyond that used here, the numerical “wall heating” affect at the origin of the domain is also sufficient to trip the EOS. Therefore it could be argued that the EOS is ultimately the limiting factor in performing HE simulations and not the *contact-coupling* in the *GhostFluid* method. However, the *contact-coupling* is clearly not helping matters and since the density perturbation is mirrored in the temperature field the approach would likely prove troublesome when using temperature-dependent reaction rates.

The “wall heating” is also responsible for the small glitch seen in the density profiles computed with the *riemann-coupling* approach. But, unlike the perturbation introduced by the *contact-coupling* it is sensitive to the initial position of the interface i.e. the further the interface is placed from the origin, where the “wall heating” originates, the smaller the glitch.

The computational results shown here are generated by a script bundled with *amr_sol::multimat*, see:

examples/tests/pbx/expansion.1

isobaric-coupling

contact-coupling

riemann-coupling

Figure 21: Computational results for an expansion-fan crossing a material interface; click to zoom in on the individual graphs. The solid lines are the control solution from the left-hand side of the computational domain. Observe how the *contact-coupling* introduces an unphysical step in the density profile, but the velocity and pressure profiles are unaffected. The *isobaric* and *riemann* couplings give comparable results.

isobaric-coupling

contact-coupling

riemann-coupling

Figure 22: Plots of $\tilde{\alpha}_1$, $\tilde{\alpha}_2$, and $\tilde{\alpha}_3$, for the expansion test. In practice all the couplings activate $\tilde{\alpha}_2$, whereas for a pure expansion it would be expected to be of zero strength. However, in accordance with the analysis, $\tilde{\alpha}_2$ for the contact-coupling is much larger than with the other two couplings. The difference between the isobaric-coupling and riemann-coupling is small.

isobaric-coupling

contact-coupling

riemann-coupling

Figure 23: The same computation as shown in Figure 12, but twice the mesh resolution. The unphysical step in density is reduced in size, however, it is still pronounced. Note that the nature of the error is such that it does not have a simple order of convergence. The error introduced per iteration certainly decreases as the mesh size decreases. But to counteract the reduction, more iterations are needed to reach a given time. Thus it is the accumulation of the error that matters, and inevitably the accumulation is controlled by non-linear effects that are beyond the scope of the present analysis.

isobaric-coupling

contact-coupling

riemann-coupling

Figure 24: Plots of $\tilde{\alpha}_1$, $\tilde{\alpha}_2$, and $\tilde{\alpha}_3$, corresponding to Figure 14. The spurious $\tilde{\alpha}_2$ is two orders of magnitude larger with the contact-coupling than it is with either the isobaric- or riemann- couplings.

isobaric-coupling

contact-coupling

riemann-coupling

Figure 25: The same computation as shown in Figure 12, but four times the mesh resolution. The unphysical density-step is still prominent, suggesting that the *contact-coupling* is deficient.

isobaric-coupling

contact-coupling

riemann-coupling

Figure 26: Plots of $\tilde{\alpha}_1$, $\tilde{\alpha}_2$, and $\tilde{\alpha}_3$, corresponding to Figure 16. The spurious $\tilde{\alpha}_2$ is again two orders of magnitude larger with the contact-coupling than it is with either the isobaric- or riemann- couplings.

Figure 27: The unphysical density-step, introduced by the *contact-coupling*, grows as the expansion-fan crosses the material interface. This time sequence is taken from the simulation shown in Figure 21.

Figure 28: The evolution of the error in density remains the same as the grid is refined. This time sequence is taken from the simulation shown in Figure 25.

3.2 Non-smooth flows

We now consider the consistency of the ghost-fluid coupling when a shock wave crosses the pseudo-material interface introduced above. The situation is more complicated than the expansion-wave case, because a shock-capturing scheme does not represent a right-moving shock-wave as an isolated acoustic i.e. while $\tilde{\alpha}_3$ is the primary wave-strength, $\tilde{\alpha}_1$ and $\tilde{\alpha}_2$ are non-vanishing. The fact that the expected passive-characteristics are active manifests itself in the familiar “start-up” errors that are generated whenever a prescribed shock-jump relaxes down to the smeared profile that a particular numerical scheme can support. Such start-up errors can also be generated when a numerical shock-profile crosses a discontinuity in mesh spacing[2]. In fact, any numerical process that perturbs a captured-shock’s equilibrium profile will result in errors that manifest themselves on the supposed passive characteristics. Therefore it would be expected that the ghost-fluid coupling would give rise to start-up errors whenever a captured-shock crosses a material interface.

Here, for brevity, we only present results for a perfect-gas, because the behaviour observed with other EOS’s is identical. Instead, it is more important to consider weak shocks separately from strong shocks, as there is a marked difference between the two cases.

3.2.1 Weak shocks

The computational setup is shown in Figure 29. The idea of this test is to introduce a material interface at a point x_i , somewhere ahead of a shock-wave which is prescribed at x_s . Thus by the time the shock reaches the interface it has settled down to its equilibrium, smeared profile. Moreover, the start-up errors have fallen sufficiently far behind the shock that they play no role in the test.

As can be seen from Figures 30-35, the contact-coupling gives markedly poorer results for the density field than either the isobaric- or riemann- couplings. Specifically, a numerical overshoot is introduced into the density profile. The velocity and pressure profiles, on the other hand, are comparable in all three cases. Figures 36 and 37 show the evolution of the numerical overshoot as the shock crosses the material interface. The results given here are for a first-order, forward-euler scheme with Lax-Friedrichs flux. But the results are representative of those obtained with higher-order methods and other flux functions. Note that as the shock is weak the analysis given for the expansion case applies.

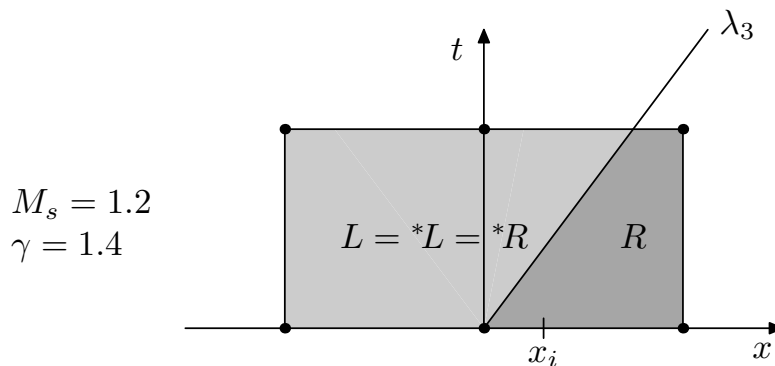


Figure 29: Schematic showing the wave pattern for the weak-shock test. The material interface is positioned at $x_i = 0$ with the shock prescribed at $x_s = -1.4$. The script for this test is bundled with `amr_sol::multimat`, see `examples/test/pg/shock.1`.

isobaric-coupling

contact-coupling

riemann-coupling

Figure 30: Computational results for an weak shock-wave crossing a material interface; click to zoom in on the individual graphs. The solid lines give the exact shock profile. Observe how the *contact-coupling* introduces an unphysical overshoot in the density profile, but the velocity and pressure profiles are unaffected. The *isobaric* and *riemann* couplings give comparable results.

isobaric-coupling

contact-coupling

riemann-coupling

Figure 31: Plots of $\tilde{\alpha}_1$, $\tilde{\alpha}_2$, and $\tilde{\alpha}_3$, for the weak-shock test. In practice all the couplings activate $\tilde{\alpha}_1$ and $\tilde{\alpha}_2$, whereas for a pure shock they would be expected to be of zero strength. However, in accordance with the analysis, $\tilde{\alpha}_2$ for the contact-coupling is much larger than with the other two couplings. The peak value of $\tilde{\alpha}_2$ for the riemann-coupling is an order of magnitude smaller than that for the contact-coupling.

isobaric-coupling

contact-coupling

riemann-coupling

Figure 32: The same computation as shown in Figure 30, but twice the mesh resolution. The overshoot in density does not diminish as there is no length scale in the problem i.e. the smeared shock profile is self-similar with mesh spacing.

isobaric-coupling

contact-coupling

riemann-coupling

Figure 33: Plots of $\tilde{\alpha}_1$, $\tilde{\alpha}_2$, and $\tilde{\alpha}_3$, corresponding to Figure 32. The peak value of $\tilde{\alpha}_2$ for the contact-coupling is two orders of magnitude larger than that for the riemann-coupling.

isobaric-coupling

contact-coupling

riemann-coupling

Figure 34: The same computation as shown in Figure 30, but four times the mesh resolution. The density overshoot with the *contact-coupling* suggests that the approach is inconsistent with the underlying PDE's. Note that as the shock is weak the isobaric-coupling, with its isentropic assumption, is not in gross error.

isobaric-coupling

contact-coupling

riemann-coupling

Figure 35: Plots of $\tilde{\alpha}_1$, $\tilde{\alpha}_2$, and $\tilde{\alpha}_3$, corresponding to Figure 34. The peak value of $\tilde{\alpha}_2$ is again two orders of magnitude larger with the contact-coupling than it is with the riemann-coupling.

Figure 36: The density overshoot, introduced by the *contact-coupling*, can be traced back to an oversteepening of the shock's density profile as it crosses the material interface. This time sequence is taken from the simulation shown in Figure 30.

Figure 37: The evolution of the error in density remains the same as the grid is refined. This time sequence is taken from the simulation shown in Figure 34.

isobaric-coupling

contact-coupling

riemann-coupling

Figure 38: Computational results for a weak-shock crossing a frozen material interface; click to zoom in on the individual graphs. The solid lines are the control solution from the left-hand side of the computational domain. Observe how the *contact-coupling* introduces an overshoot in the density profile, but the velocity and pressure profiles are unaffected. The results with the *riemann-coupling* are marginally better than those with the *isobaric-coupling*.

3.2.2 Strong shocks

The computational setup for the strong shock-wave case is shown in Figure 39. The situation is the same as before, except that the shock Mach number has been increased from 1.2 to 10. As can be seen from Figures 40-45, all the ghostfluid couplings now exhibit an overshoot in the density field. The overshoot with the contact-coupling, however, is clearly larger than those with the other couplings. Figures 46 and 47 show the evolution of the numerical overshoot as the shock crosses the material interface. Again, the results given here are for a first-order, forward-euler scheme with Lax-Friedrichs flux. But the results are representative of those obtained with higher-order methods and other flux functions.

Figure 48 shows the results when the interface is frozen. The results for the isobaric- and riemann-couplings are similar, but something is clearly amiss. The analysis for the expansion case no longer applies, given the strength of the shock. But the source of the error seen in Figure 48 is not hard to find. Consider Figure 3. For a single material calculation, the flux across AD is the same for both cells $ABCD$ and $ADC'B'$. Specifically, it is $\mathbf{F}(\mathbf{W}_{*L})$. But in the two-material simulation shown in Figure 48, with riemann-coupling: the left-hand cell uses $\mathbf{F}(\mathbf{W}_{*L})$ and the right-hand cell uses $\mathbf{F}(\mathbf{W}_{*R})$. Now for a single right-moving shock, \mathbf{W}_{*L} and \mathbf{W}_{*R} should be the same and so the discrepancy should not matter. But for a numerically-smearred shock, the star states are not the same. And for the strength of shock used here, there is a sizeable difference³. Thus the right-hand cell uses a flux which is in gross error, while that for the left-hand cell is correct. This explains why the profile seen in Figure 48 is correct on the left-hand side of the interface, but incorrect on the right-hand side. When the interface is allowed to move, the error is much reduced. But it still retains its lop-sided nature as can be seen by examining the riemann-coupling, density-profile in Figure 44.

It is relatively straightforward to devise a ghostfluid prescription that passes the present strong-shock test with flying colours. For an examination of the functional form for Equation 11 suggests that all one need do is to apply an isobaric prescription with the constraint $\rho c = \text{constant}$, rather than the normal isentropic constraint. Then the two-material simulation reduces identically to the one-material simulation, which has been confirmed by numerical testing. However such an impedance-coupling fails when the left and right materials are different, thus undermining its usefulness.

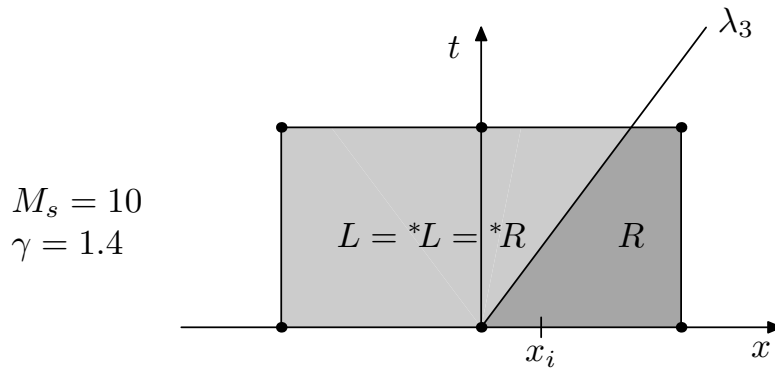


Figure 39: Schematic showing the wave pattern for the strong-shock test. The material interface is positioned at $x_i = 0$ with the shock prescribed at $x_s = -1.4$. The script for this test is bundled with `amr_sol::multimat`, see `examples/test/pg/shock.1`.

³In the weak-shock case the difference between the star states is sufficiently small that the discrepancy in the choice of fluxes does not matter.

isobaric-coupling

contact-coupling

riemann-coupling

Figure 40: Computational results for a strong shock-wave crossing a material interface; click to zoom in on the individual graphs. The solid lines give the exact shock profile. For a strong shock all three couplings give an overshoot in density, although the overshoot with the *contact-coupling* is significantly larger than that for either the *isobaric*- or *riemann*- couplings. The *contact-coupling* also now has an overshoot in the pressure field.

isobaric-coupling

contact-coupling

riemann-coupling

Figure 41: Plots of $\tilde{\alpha}_1$, $\tilde{\alpha}_2$, and $\tilde{\alpha}_3$, for the strong-shock test. Observe how $\tilde{\alpha}_2$ is now non-small compared to $\tilde{\alpha}_1$ for all three of the couplings. This is true, however, for the smeared-shock even before it gets to the material interface and it is what distinguishes the strong-shock case from the weak-shock one.

isobaric-coupling

contact-coupling

riemann-coupling

Figure 42: The same computation as shown in Figure 40, but twice the mesh resolution. The overshoot in density does not diminish as there is no length scale in the problem i.e. the smeared shock profile is self-similar with mesh spacing. The density overshoot for the isobaric case looks like it has diminished, but this is merely a consequence of the specific frame picked out from the simulation.

isobaric-coupling

contact-coupling

riemann-coupling

Figure 43: Plots of $\tilde{\alpha}_1$, $\tilde{\alpha}_2$, and $\tilde{\alpha}_3$, corresponding to Figure 42.

isobaric-coupling

contact-coupling

riemann-coupling

Figure 44: The same computation as shown in Figure 40, but four times the mesh resolution. The density overshoot for the riemann-coupling can be reduced slightly by replacing the present linearized solver with an exact riemann solver. But the source of the overshoot cannot be eliminated, as it ultimately arises from the choice of control-volume used by the ghost-fluid method.

isobaric-coupling

contact-coupling

riemann-coupling

Figure 45: Plots of $\tilde{\alpha}_1$, $\tilde{\alpha}_2$, and $\tilde{\alpha}_3$, corresponding to Figure 44.

Figure 46: The density overshoot, introduced by the *contact-coupling*, can be traced back to an oversteepening of the shock's density profile as it crosses the material interface. This time sequence is taken from the simulation shown in Figure 40.

Figure 47: The evolution of the error in density remains the same as the grid is refined. This time sequence is taken from the simulation shown in Figure 44.

isobaric-coupling

contact-coupling

riemann-coupling

Figure 48: Computational results for a strong-shock crossing a frozen material interface; click to zoom in on the individual graphs. The results for the isobaric- and riemann- coupling now give nonsense, but this can be explained by the fact the smeared shock now carries with it what amount to a sequence of mini contact-surfaces. And when these contacts cross the frozen material-interface, a sizeable error is introduced because the flux for the right hand material is computed using \mathbf{W}_{*R} rather than \mathbf{W}_{*L} as would be the case for a true single-material simulation.

4 Closing comments

This note identifies a number of intrinsic weaknesses of the ghostfluid method. The nature of the weaknesses helps explain the hit-and-miss experience, where sometimes the ghostfluid method works quite nicely and other times it fails miserably. The popularity of the method is undoubtedly due to the ease with which it can be implemented and the fact that its inherent weaknesses are not exposed in a number of applications of interest.

The numerical evidence presented here is far from exhaustive, but `amrprogamr_sol::multimat` can be used to pose follow-up questions. For example, it should be realised that the perturbations generated by the ghostfluid method, say as a shock crosses a material interface, can be sufficient to trip an EOS that has a limited domain of dependence. And while tuning the flavour of ghostfluid coupling can sometimes help matters, the perturbations are symptomatic of deeper problems. The real failing of the ghostfluid algorithm lies with its choice of control-volumes, which can, depending on the data involved, be a poor approximation to the lagrangian control-volumes needed at material boundaries.

The recommendation here is that an HE group discussion is needed to determine whether or not the ghostfluid method constitutes a viable, long-term simulation tool. For example, the evidence given here suggests that the method will not be able to cope with shock-initiation problems that employ temperature-dependent reaction rates. And it is to be hoped that a group discussion would bring out any other issues that remain to be addressed.

References

- [1] FEDKIW, R. P., ASLAM, T. D., MERRIMAN, B., AND OSHER, S. 1999 A Non-oscillatory Eulerian Approach to Interfaces in Multimaterial Flows (the Ghost Fluid Method). *J. Comput. Phys.* **152**, pp. 457–492.
- [2] QUIRK, J. J. 1991 An Adaptive Mesh Refinement Algorithm for Computational Shock-Hydrodynamics. Ph.D. Thesis, College of Aeronautics, Cranfield Institute of Technology.
- [3] ROE, P. L. 1981 Approximate Riemann Solvers, Parameter Vectors, and Difference Schemes. *J. Comput. Phys.* **43**, pp. 357–372.
- [4] ROE, P. L. AND PIKE, J. 1984 Efficient Construction and Utilisation of Approximate Riemann Solutions. *Comput. Math. Appl. Sci. & Eng.* **VI**, eds. Glowinski, R. and Lions, J-L., pp. 499–518.
- [5] ROE, P. L. 1986 Characteristic-Based Schemes for the Euler Equations. *Ann. Rev. Fluid. Mech.* **18**, pp. 337–365.